PHYSICAL REVIEW A **00**, 002800 (2026)

Experimental determination of L-subshell x-ray production cross sections for La, Ce, Pr, and Nd by electron impact

Judith Guzmán, Alejo Carreras, Jorge Trincavelli, Silvina Segui, Gustavo Castellano, and Silvina Limandri[*]
Instituto de Física Enrique Gaviola (IFEG-CONICET), Facultad de Matemática, Astronomía, Física y Computación (FAMAF),
Universidad Nacional de Córdoba, Córdoba, Argentina

(Received 30 December 2025; accepted 24 February 2026; published xxxxxxxxxx)

L-subshell x-ray production cross sections induced by electron impact were determined for La, Ce, Pr, and Nd in the incidence energy range of 5.7–25 keV. The experiments were carried out by irradiating thick samples in a field-emission scanning electron microscope equipped with an energy-dispersive spectrometer. The x-ray spectra were then analyzed using a previously developed optimization software, which accounts for bulk effects through a model for the ionization depth distribution function. The x-ray production cross sections obtained were compared with theoretical predictions, using different relaxation data reported in the literature. A good agreement is obtained for the L_2 and L_3 subshells when the distorted-wave Born approximation model is used along with the relaxation parameters reported by Perkins *et al.* [Technical Report UCRL-50400, Vol. 30, Lawrence Livermore National Laboratory, Livermore, CA, 1991]. However, for the L_1 subshell, the theoretical curves systematically underestimate the measurements in the high-energy region, evincing the need for further determinations of the fluorescence yield coefficient for this subshell.

DOI: 10.1103/b4b5-cp4j

I. INTRODUCTION

Knowledge of inner-shell ionization cross sections by electron impact is crucial in many areas of both basic and applied physics. Reliable values of these cross sections are required, for instance, to perform realistic calculations of correction factors for the x-ray intensities in electron probe microanalysis, to model electron and photon radiation transport in Monte Carlo simulations, and to develop analytical descriptions of electron-induced x-ray spectra.

Despite decades of extensive experimental and theoretical efforts, a complete understanding of how inner-shell ionization cross sections depend on the atomic number and the incident electron energy remains elusive. Theoretical models such as the plane-wave Born approximation [1] or a more refined formalism using the distorted-wave Born approximation (DWBA) [2] provide predictions for these quantities; however, their accuracy can only be evaluated through comparison with experimental data.

For the K shell, many elements and energy ranges have already been addressed by experimental determinations. In a recent work [3], 2509 experimental data points were compiled, although some elements and energy ranges still have to be explored.

The situation of L shells is significantly more limited. No data exist for numerous elements along the periodic table. Particularly for lanthanides, the number of available experimental results is very scarce [4]. This lack of reliable measurements is mainly due to the fact that the energy spacing between L_1, L_2, and L_3 subshells frequently produces line overlappings for each of these elements, which hinders the appropriate deconvolution of the emission lines involved—particularly relevant when an energy-dispersive spectrometer is used in the experiment. In addition, in this region of the periodic table, Coster-Kronig transition probabilities become quite important, and the atomic relaxation data necessary to compare with theoretical models for ionization cross sections are determinant [5,6]. No data are available in the literature for Pm and Tb, while for La, Ce, Pr, Nd, Eu, Er, and Yb, the existing scarce measurements are limited to a few relativistic energies [7–10]. Although a larger volume of data can be found for Sm, Gd, Dy, Ho, and Tm [7–9,11–17], in each case there are no measurements in the same energy range by different authors which would validate the trends observed. Recent data for Lu $L\alpha$ and $L\beta$ have also been reported for a single electron energy [18]. Given the limited amount of measurements available for keV electrons, a comparison between different theoretical models is very difficult to perform. This underlines the need for further experimental determinations.

The properties of rare-earth elements have been the subject of increasing interest in recent decades due to the multiple applications of materials containing these elements. Some examples include the use of Nd in permanent magnets [19] and of several rare-earth elements in the petroleum industry [20], in catalysis [21], in manufacturing of nickel-metal hydride batteries, which are widely used in hybrid and electric vehicles [22], etc.

In this work, x-ray production cross sections for the L_1, L_2, and L_3 subshells of La, Ce, Pr, and Nd by electrons impact in the 5.7–25 keV incidence energy range were experimentally determined. To this aim, x-ray spectra acquired from bulk standards were processed through a careful methodology, implemented in a software previously developed [23]. The

---

[*] Contact author: slimandri@unc.edu.ar

2469-9926/2026/00(0)/002800(9)

results are compared with theoretical calculations of ionization cross sections converted to x-ray production cross sections by using different sets of fluorescence yields and Coster-Kronig transition probabilities.

II. EXPERIMENTAL

The x-ray emission spectra induced by electron impact were obtained from lanthanide thick solid standards (Micro-Analysis Consultants LTD): LaB_6, $CeAl_2$, PrF_3, and NdF_3 for lanthanum, cerium, praseodymium, and neodymium, respectively. According to the standard certificates, sample impurities are lower than 0.5 wt% in all cases, so their influence on the x-ray spectra can be neglected. The standards are mounted on a nonconductive resin inside a brass block coated with a carbon thin layer to ensure adequate thermal and electrical conductivity.

The targets were irradiated with an electron beam in a Carl Zeiss Σigma field emission scanning electron microscope. The x-ray spectra were acquired by means of an energy-dispersive spectrometer based on an Oxford silicon drift detector with an AZtec characterization system, whose front window is an ultrathin polymer layer, supported by a 380-μm-thick silicon grid with 77% open area. The detector intrinsic efficiency ϵ was determined in a previous work [24].

The incident electron energies E_o used were between 5.7 and 25 keV. The beam currents used, measured with a Faraday cup before and after recording each spectrum, ranged from 120 to 1700 pA, with beam fluctuations below 1.5%.

III. METHODOLOGY

The spectra were processed by means of the software POEMA [23], which has been previously developed and successfully applied for determining x-ray production cross sections for K, L, and M shells in several elements [5,6,24–26]. The method implemented in this software involves the minimization of the (weighted) quadratic differences χ^2 between the experimental spectrum and an analytic function depending on refinable instrumental and atomic parameters; among these atomic parameters, attention is focused on the x-ray production cross sections. A brief overview of the expressions used to describe each spectrum is provided in the next section, and a more detailed description can be found in Ref. [24].

A. Spectral description

The analytic expression considered to account for the x-ray intensity $\tilde{I}_n$ at the nth channel can be written as

$$\tilde{I}_n = B(E_n) + \sum_{\nu kq} P_{\nu kq} S_{\nu kq}(E_n), \qquad (1)$$

where $B(E_n)$ corresponds to the background intensity contribution at the energy E_n of the nth channel [27], and P and S are, respectively, the intensity and the function employed for describing the peak profile—a Gaussian function for the spectrometer used in this work. For each element ν in the irradiated sample, k refers to the atomic shell where the primary vacancy associated with the characteristic line q occurs. For a mass concentration C_ν and a beam current i running during a live acquisition interval Δt, the intensity factor $P_{\nu kq}$ in Eq. (1) is expressed as

$$P_{\nu kq} = \frac{i\Delta t}{e} C_\nu \sigma^{\mathrm{x}}_{\nu k}\, p_{\nu kq}\, (ZAF)_{\nu kq}\, \epsilon(E_{\nu kq}) \frac{\Delta\Omega}{4\pi}, \qquad (2)$$

where e is the elementary charge; $E_{\nu kq}$ is the q-line characteristic energy; $p_{\nu kq}$ is the corresponding relative transition probability (RTP); the matrix correction factors Z, A, and F are related to the so-called atomic number, absorption, and fluorescence corrections [28], respectively; $\epsilon(E_{\nu kq})$ is the detection intrinsic efficiency; $\Delta\Omega/(4\pi)$ is the solid angle fraction subtended by the detector [24]; and $\sigma^{\mathrm{x}}_{\nu k}$ is the x-ray production cross section for the k subshell of interest at the incident electron energy E_o. The software estimates the Z, A, and F factors by using the ionization depth distribution function, for which the modified Gaussian model proposed by Packwood and Brown [29], with parameters given by Riveros and Castellano [30], is used, whereas the F factor is assessed according to the traditional Reed's model [31], although it is negligible for the samples involved in the present work.

The effect of the carbon coating, related to the attenuation and energy loss of the incident electrons and to the absorption of the emitted x-rays, is properly accounted for by the software according to a previous study based on Monte Carlo simulations [32]. To determine the carbon coating thickness, an x-ray spectrum originating in a region of the brass support close to the standards used was recorded and fitted with the software. As a result of the fitting, a value of 8.4 ± 0.3 nm for the carbon coating thickness was obtained.

After traversing the surface carbon layer, the actual energy E_o of the incoming electrons may differ from the nominal value for several reasons, including energy loss in the carbon film, calibration of the electron beam energy, and minor charging effects that are not fully compensated by the conductive coating. To account for the latter two issues, the Duane-Hunt limit E_{DH} [33] was determined as the maximum energy of the detected bremsstrahlung photons in each spectrum. The energy loss due to the coating was estimated using the software [32], with E_{DH} as input. The effective incident energies differ from the nominal values by 1.6% or less in all cases.

B. Fitting strategy

For each element, the spectrum acquired at 20 keV was fitted in first place. To this aim, initial values for the characteristic x-ray energies and the relative transition probabilities were taken from the compilations by Bearden [34] and Perkins *et al.* [35], respectively, and some of them were optimized to attain a better description of the spectrum. The remaining spectra were then fitted using the values obtained for these parameters, which were kept fixed during the optimization procedure.

In all cases, the characteristic peak widths were obtained through the refinement of two global instrumental parameters corresponding to the spectrometer noise and the Fano factor associated with the detection system. In addition, the *zero* and *gain* calibration parameters, as well as the background scale factor, were also optimized for each spectrum. The contribution of these five parameters to the cross-section

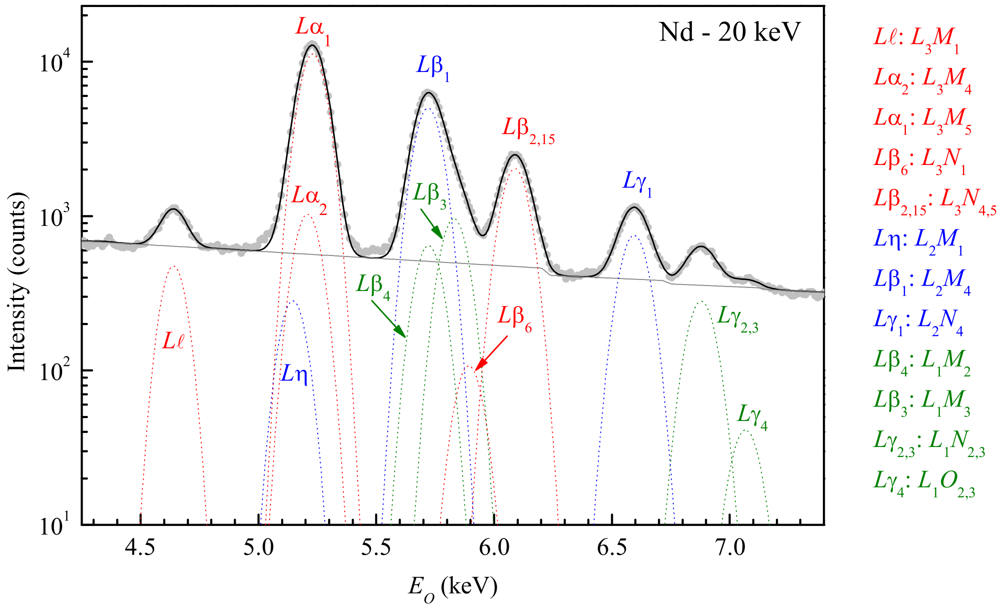

FIG. 1. X-ray spectrum for Nd at 20-keV incidence energy. Gray circles: experimental; solid black line: fit; solid gray line: background; isolated peaks (dotted lines): characteristic decays to L3 (red), L2 (blue), and L1 (green) shells. The corresponding transitions for the lines detected are listed on the right side.

uncertainties is negligible. Particularly, noise, Fano factor, and *zero* and *gain* calibration parameters were determined with high precision, since the fit quality is highly sensitive to these parameters. On the other hand, the background scale factor had a minor influence on the cross section values. Finally, as a result of the fitting procedure, the x-ray production cross section values $\sigma^x_{\nu k}$ for L_1, L_2, and L_3 subshells were obtained for each element and incidence energy.

IV. RESULTS AND DISCUSSION

Figure 1 shows, as an example, the experimental spectrum for Nd at 20 keV, along with the analytical description and the corresponding background and characteristic-line contributions. As can be seen, a very good fit was achieved; in all cases, similar spectral structures and fitting qualities were found.

As explained in Sec. III B, the optimization process followed to determine the x-ray production cross sections involved the refinement of some characteristic energies and RTPs in the 20-keV spectra. The values obtained for these parameters are shown in Tables I and II, respectively.

Regarding the six characteristic energies determined, a general agreement between the present data and those reported by Bearden [34] can be observed. Nevertheless, some discrepancies arise in La and Ce for the $L\gamma_{2,3}$ line, and in Pr and Nd for the $L\ell$ line. It must be emphasized that these transitions—particularly the $L\ell$ decay—exhibit peaks that are not overlapped with other structures and are intense enough to allow for a reliable determination. Some lines could not be characterized due to their weakness. In those cases, characteristic energies and RTPs were taken from the literature [34,35] to carry out the fitting procedure.

In general terms, the RTPs determined show good agreement with those reported by Perkins *et al.* [35]. The main exception corresponds to the $L\ell$ line, for which the present values are less than half of the data published in Ref. [35] for the four elements studied. Scofield [36] determined RTP values for Nd and obtained RTP $= 0.015$ for the $L\ell$ line, quite below the present result. This suggests that the theoretical predictions for this particular transition rate are not

TABLE I. Characteristic x-ray energies in keV, obtained as a result of the optimization process along with values reported by Bearden [34]. Numbers in parentheses indicate the estimated uncertainties in the last digits.

	La		Ce		Pr		Nd	
Transition	This work	Ref. [34]	This work	Ref. [34]	This work	Ref. [34]	This work	Ref. [34]
$L_1N_{2,3}$ ($\gamma_{2,3}$)	6.054(3)	6.060(1)	6.316(2)	6.325(1)	6.599(2)	6.598(1)	6.879(3)	6.883(2)
$L_1O_{2,3}$ (γ_4)	6.23(2)	6.252(1)	6.55(1)	6.528(1)	6.81(1)	6.815(2)	7.07(1)	7.107(2)
L_2M_4 (β_1)	5.0409(4)	5.0421(1)	5.2602(5)	5.2622(7)	5.4881(5)	5.4889(7)	5.7194(6)	5.7216(5)
L_2N_4 (γ_1)	5.786(1)	5.7885(8)	6.048(1)	6.052(1)	6.317(1)	6.322(1)	6.595(1)	6.6021(7)
L_3M_1 (ℓ)	4.123(2)	4.124(4)	4.289(2)	4.2875(6)	4.465(2)	4.4532(6)	4.639(2)	4.6330(7)
$L_3N_{4,5}$ ($\beta_{2,15}$)	5.3810(7)	5.3835(7)	5.6104(7)	5.6134(5)	5.8499(7)	5.850(1)	6.0877(8)	6.0894(9)

TABLE II. RTPs obtained as a result of the optimization process along with values reported by Perkins *et al.* [35]. Numbers in parentheses indicate the estimated uncertainties in the last digits.

	La		Ce		Pr		Nd	
Transition	This work	Ref. [35]	This work	Ref. [35]	This work	Ref. [35]	This work	Ref. [35]
$L_1M_{2,3}$ ($\beta_{3,4}$)[a]	0.83(1)	0.789	0.80(1)	0.789	0.80(1)	0.788	0.81(1)	0.787
$L_1N_{2,3}$ ($\gamma_{2,3}$)	0.160(9)	0.184	0.184(7)	0.184	0.180(7)	0.185	0.166(8)	0.186
$L_1O_{2,3}$ (γ_4)	0.010(4)	0.027	0.016(3)	0.027	0.020(4)	0.027	0.024(5)	0.027
L_2M_1 (η)	0.034(3)	0.039	0.035(4)	0.038	0.021(2)	0.036	0.045(8)	0.035
L_2M_4 (β_1)	0.84(2)	0.823	0.83(2)	0.825	0.85(2)	0.819	0.82(2)	0.826
L_2N_4 (γ_1)	0.131(4)	0.138	0.134(3)	0.137	0.132(3)	0.137	0.138(5)	0.140
L_3M_1 (ℓ)	0.031(1)	0.072	0.032(1)	0.069	0.032(1)	0.067	0.032(1)	0.065
$L_3M_{4,5}$ ($\alpha_{1,2}$)[a]	0.82(3)	0.791	0.82(3)	0.793	0.82(2)	0.793	0.82(3)	0.795
$L_3N_{4,5}$ ($\beta_{2,15}$)	0.140(3)	0.129	0.137(2)	0.129	0.135(2)	0.130	0.138(3)	0.131

[a] These two lines were processed jointly.

thoroughly trustworthy. On the other hand, the present experimental results appear to be reliable, given that the $L\ell$ line is not overlapped and is sufficiently intense, as can be observed in Fig. 1. Note that both the $L\alpha_1$ and $L\alpha_2$ lines and the $L\beta_3$ and $L\beta_4$ lines were treated jointly due to their proximity, maintaining their intensity ratios to coincide with those found in the literature.

The x-ray production cross section values obtained as a result of the spectral processing are presented in Table III, along with the nominal incidence energy, the Duane-Hunt limit, and the effective electron energy after crossing the carbon conductive layer. The relative uncertainty in the x-ray production cross section was estimated as the quadrature sum of the relative uncertainties in the main error sources in Eq. (2), i.e., the net predicted characteristic intensities, the *ZA* factors, and the solid angle $\Delta\Omega$ (the uncertainty in the beam current and the intrinsic detector efficiency do not contribute significantly to the overall error). The uncertainty in the peak intensities was assessed by analyzing the fit quality when varying global peak scale factors embracing decays to each subshell. In addition, the uncertainty associated with the matrix correction factors was estimated from the variation in the x-ray production cross sections due to the differences in the *Z* and *A* factors obtained by using two parametrizations of the Gaussian model of Packwood and Brown [29]: the one suggested by Riveros and Castellano [30] and that by Bastin

TABLE III. X-ray production cross sections for the *L* subshells of La, Ce, Pr, and Nd. The second column corresponds to the nominal incidence energy, the third one is the Duane-Hunt limit, and the fourth column represents the electron energy after traversing the carbon conductive layer. Numbers in parentheses indicate the estimated uncertainties in the last digits.

	E (keV)	E_{DH} (keV)	E_o (keV)	$\sigma^{\mathrm{x}}_{L_1}$ (barns)	$\sigma^{\mathrm{x}}_{L_2}$ (barns)	$\sigma^{\mathrm{x}}_{L_3}$ (barns)		E (keV)	E_{DH} (keV)	E_o (keV)	$\sigma^{\mathrm{x}}_{L_1}$ (barns)	$\sigma^{\mathrm{x}}_{L_2}$ (barns)	$\sigma^{\mathrm{x}}_{L_3}$ (barns)
La	25	24.78	24.76	47(4)	130(9)	290(20)	Ce	25	24.76	24.73	47(3)	132(8)	290(20)
	20	19.82	19.79	49(3)	141(8)	320(20)		20	19.91	19.88	48(3)	140(7)	310(20)
	15	14.87	14.83	50(3)	158(9)	370(20)		15	14.95	14.91	48(3)	140(8)	330(20)
	12	11.87	11.82	47(4)	150(10)	350(20)		12	11.94	11.89	41(3)	130(8)	310(20)
	10	10.08	10.02	38(3)	119(9)	300(20)		10	10.12	10.06	32(3)	102(8)	250(20)
	8	8.04	7.97	24(3)	75(8)	210(20)		8	8.16	8.09	14(2)	59(7)	160(20)
	7	7.07	6.97	5(1)	41(6)	140(20)		7	7.09	7.01	6(1)	25(4)	100(10)
	6.7	6.78	6.70	1.2(7)	27(5)	96(16)		6.7	6.82	6.74		12(3)	70(10)
	6.5	6.57	6.48	0.3(6)	19(3)	86(15)		6.5	6.59	6.50		8(2)	60(10)
	6.2	6.29	6.20		6(1)	58(12)		6.2	6.28	6.19			34(8)
	5.9	5.99	5.90			30(7)		5.9	5.96	5.87			11(3)
	5.7	5.77	5.67			13(4)							
Pr	25	24.62	24.60	47(3)	139(8)	300(20)	Nd	25	24.79	24.77	51(4)	134(9)	300(20)
	20	19.77	19.74	50(2)	145(7)	330(10)		20	19.92	19.89	49(3)	141(8)	310(20)
	15	15.01	14.97	45(3)	142(7)	320(20)		15	15.00	14.96	47(3)	137(8)	320(20)
	12	11.92	11.87	39(3)	130(7)	310(20)		12	11.92	11.87	43(3)	122(7)	290(20)
	10	10.12	10.06	30(2)	98(6)	250(20)		10	10.10	10.04	28(2)	90(6)	230(20)
	8	8.09	8.02	15(2)	50(5)	150(20)		8	8.06	7.99	9(1)	30(5)	130(20)
	7	7.07	6.99		19(3)	80(10)		7	7.14	7.06		4(2)	60(10)
	6.7	6.83	6.75		7(1)	50(10)		6.7	6.86	6.78			34(7)
	6.5	6.60	6.51			40(8)		6.5	6.57	6.48			20(5)
	6.2	6.30	6.21			16(4)							

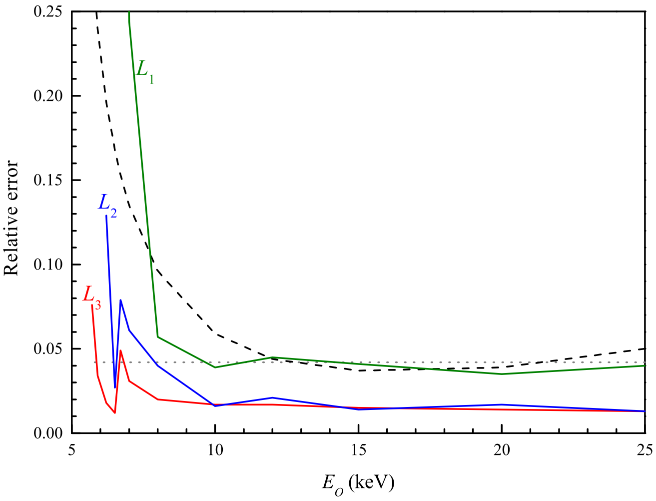

FIG. 2. Main contributions to the uncertainties of lanthanum x-ray production cross sections. Solid angle: gray dotted line, *ZAF* factors: black dashed line. Global peak scale factors: color solid lines (L_1, green; L_2, blue; L_3, red).

et al. [37]. Finally, the solid angle fraction subtended by the detector and the corresponding uncertainty were determined in a previous work as $\Delta\Omega/(4\pi) = 0.0024 \pm 0.0001$ [24].

The contributions of the different error sources for the case of lanthanum are shown in Fig. 2 as an example—a similar behavior was found for the other elements. It can be seen that the main contribution corresponds to the model used to assess the *ZA* corrections, except for the L_1 group, where the error introduced by the peak scale factor is the most important for low incidence energies and becomes comparable at intermediate and high E_o values.

In order to compare experimental results with theoretical prediction, the theoretical predicton for the ionization cross sections must be transformed into x-ray production cross sections. For the element j in the sample, the x-ray production cross section corresponding to the L_i subshell, $\sigma^{\mathrm{x}}_{L_i} \equiv \sigma^{\mathrm{x}}_{\nu L_i}$, can be written as

$$\sigma^{\mathrm{x}}_{L_i} = \omega_{L_i}\,\tilde{\sigma}_{L_i},$$

where ω_{L_i} is the fluorescence yield and $\tilde{\sigma}_{L_i}$ is the final vacancy production cross section, which in turn can be expressed in terms of the ionization cross sections σ_{L_i} as follows:

$$\begin{aligned}\tilde{\sigma}_{L_1} &= \sigma_{L_1},\\ \tilde{\sigma}_{L_2} &= \sigma_{L_2} + f_{12}\sigma_{L_1},\\ \tilde{\sigma}_{L_3} &= \sigma_{L_3} + f_{13}\sigma_{L_1} + f_{23}(\sigma_{L_2} + f_{12}\sigma_{L_1}),\end{aligned}$$

with f_{ij} being the probability of a vacancy migration from L_i to L_j subshells through a Coster-Kronig transition. Table IV lists the values of ω_{L_i} and f_{ij} given by different authors and considered in this work.

Figures 3 and 4 show a comparison of the present results with the calculations of Bote *et al.* [40] performed on the basis of the DWBA, using the datasets for ω_{L_i} and f_{ij} given in Table IV. A reasonably good agreement is obtained for L_2 and L_3 subshells, particularly when the DWBA theoretical model is combined with the relaxation parameters given by Perkins *et al.* [35]. For these subshells, the same behavior is observed for all the studied elements: the theoretical curves overestimate the cross sections at low energies, especially near the binding energy, where the performance of the parametrization proposed by Bote *et al.* [40] is less accurate, and the original DWBA model presents numerical difficulties [41]. For higher energies ($E \gtrsim 10$ keV), the agreement improves and the experimental data lie within the band determined by the theoretical curves considering one standard deviation. In some cases (Pr-L_2 and Nd-L_2), the models slightly underestimate the measurements, although they lie within the experimental error bars.

TABLE IV. Fluorescence yields and Coster-Kronig coefficients taken from the literature to convert σ_{L_i} values into $\sigma^{\mathrm{x}}_{L_i}$ values.

Element	Ref.	ω_{L_1}	ω_{L_2}	ω_{L_3}	f_{12}	f_{13}	f_{23}
La	[35]	0.0544	0.111	0.111	0.203	0.332	0.180
	[38]	0.055	0.103	0.104	0.19	0.29	0.153
Ce	[35]	0.0574	0.119	0.118	0.206	0.332	0.176
	[38]	0.058	0.110	0.111	0.19	0.29	0.153
Pr	[35]	0.0604	0.127	0.125	0.208	0.333	0.174
	[38]	0.061	0.117	0.118	0.19	0.29	0.153
Nd	[35]	0.0635	0.136	0.132	0.209	0.333	0.172
	[38]	0.064	0.124	0.125	0.19	0.30	0.152
	[39]	0.0746	0.133	0.135	0.207	0.303	0.141

For the L_1 subshell, the theory also overestimates the cross section at low energies. However, in the higher-energy region, only the Nd curve obtained using McGuire's fluorescence yield [39] gets closer to the experimental values; the general trend is to underestimate the experimental data, being more pronounced when using the atomic relaxation parameter sets given by Perkins *et al.* [35] and Krause [38]—with differences of up to ∼30% in some cases. Nevertheless, it must be noticed that the results obtained for the L_1 group appear to be reliable, since this group presents a strong characteristic line that does not overlap with others (see the $L\gamma_{2,3}$ line in Fig. 1). In addition, even though the $L\beta_3$ and $L\beta_4$ decays—to the L_1 shell—overlap with the $L\beta_1$ peak, the corresponding $\sigma^{\mathrm{x}}_{L_2}$ values are in very good agreement with the theoretical data, which suggests that the deconvolution process has been successfully carried out. It is worth noting that for the L_1 subshell, only the fluorescence yield ω_{L_1} is needed for converting the theoretical ionization cross section into an x-ray production cross section. DWBA calculations have been proven to describe reasonably well the scarce experimental data available for the L-subshell ionization cross sections [42–45], which suggests that the origin for these discrepancies must be attributed to the fluorescence yield ω_{L_1}. As can be seen in Fig. 5, in the atomic number range of interest, the published data are scarce; particularly, the values recommended by Campbell [46] for higher atomic numbers support the ω_{L_1} trend reported by McGuire [39] in the lanthanide range.

V. CONCLUSION

In this work, experimental values of the electron-impact-induced L-subshell x-ray production cross sections of La,

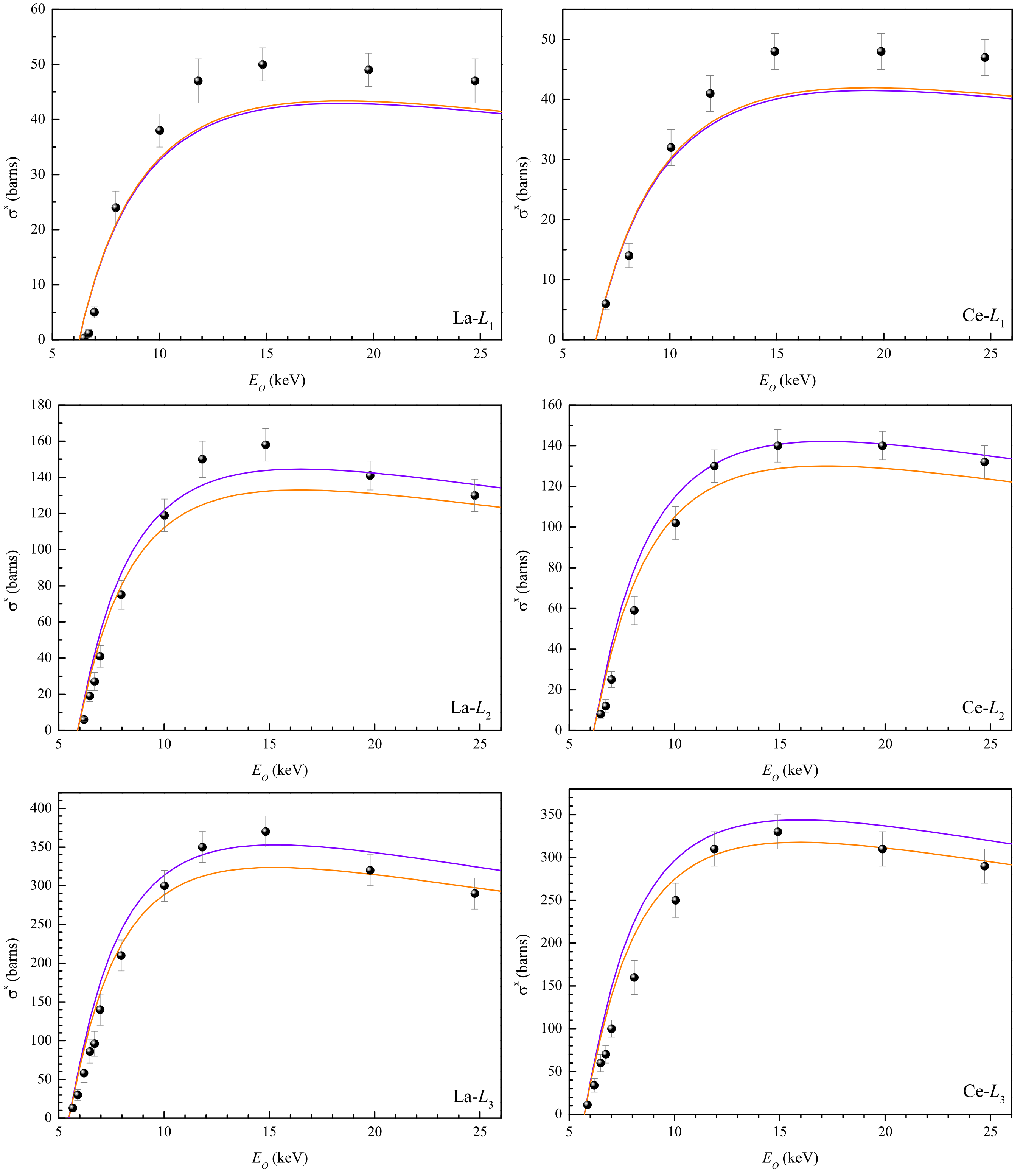

FIG. 3. X-ray production cross sections for La and Ce. Spheres: present experimental results; lines: data derived from ionization cross-section values calculated by means of a DWBA-based model [2] converted to x-ray production cross sections using different sets of ω_{L_i} and f_{ij} parameters: Ref. [35] (violet), Ref. [38] (orange).

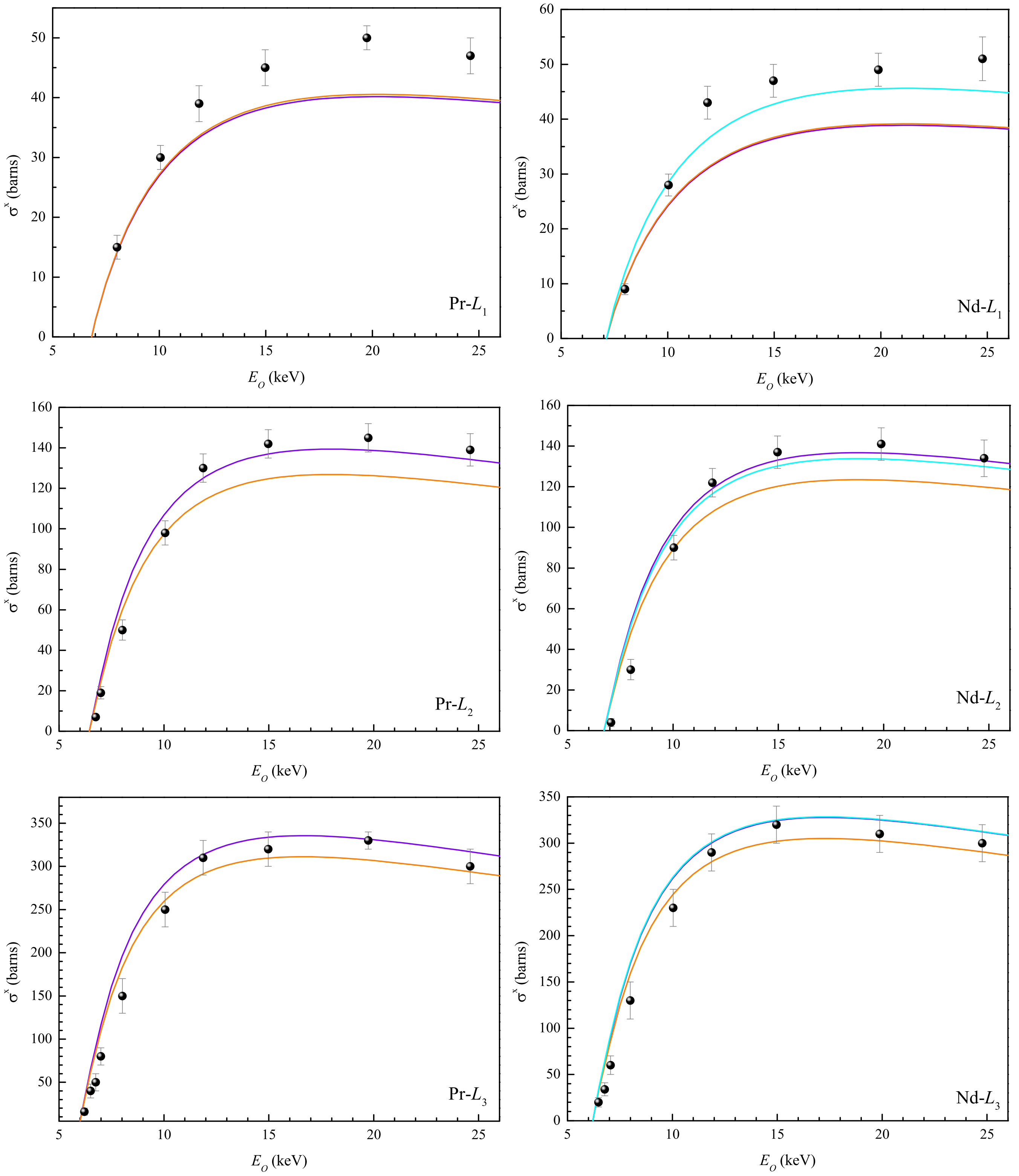

FIG. 4. X-ray production cross sections for Pr and Nd. Spheres: present experimental results; lines: data derived from ionization cross-section values calculated by means of a DWBA-based model [2] converted to x-ray production cross sections using different sets of ω_{L_i} and f_{ij} parameters: Ref. [35] (violet), Ref. [38] (orange), and Ref. [39] (cyan).

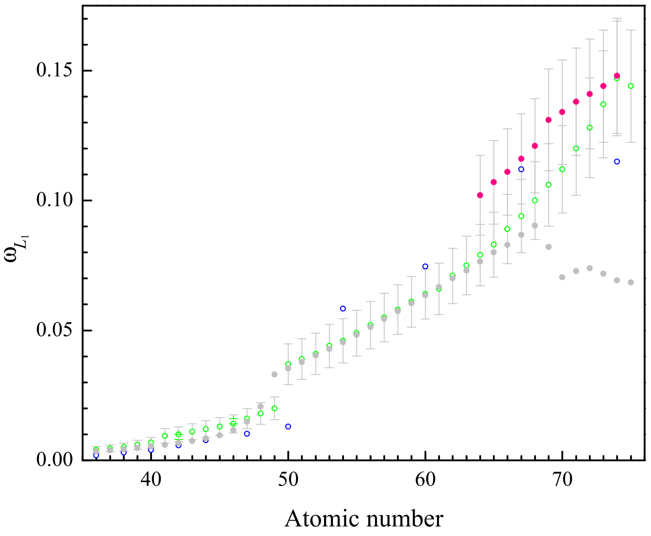

FIG. 5. Theoretical datasets for the L_1 x-ray fluorescence yields ω_{L_1}, as a function of the atomic number. Gray solid symbol: Perkins *et al.* [35]; green empty symbol: Krause [38]; blue empty symbol: McGuire [39]; red solid symbol: Campbell [45].

Ce, Pr, and Nd were determined for incidence energies between 5.7 and 25 keV. The results obtained show a general good agreement with the DWBA theoretical model within the spread related to the dispersion of the relaxation parameters required to convert ionization into x-ray production cross sections, except for the L_1 subshell. In this case, the theoretical curves systematically underestimate the measurements for $E > 10$ keV, which might be attributed to incorrect values of the fluorescence yield ω_{L_1}. The scarcity of experimental data for lanthanides and their great dispersion observed for larger atomic numbers encourage further investigations to obtain reliable estimates for this parameter.

Regarding the characteristic energies and RTPs, the obtained results are in good agreement with the data published by other authors, except for some particular cases discussed above.

This work provides useful data for the evaluation of theoretical models of ionization-relaxation mechanisms, particularly within the atomic number range studied, given the scarcity of experimental L-subshell x-ray cross sections for rare-earth elements. In future contributions, measurements in heavier rare-earth elements could be performed to extend the present study.

Although the methodology used in this work has already been applied to the determination of x-ray production cross sections in pure bulk samples, it is worth emphasizing that along the present work compound samples have successfully been studied. This evidences the robustness of the previously developed parameter optimization methodology.

ACKNOWLEDGMENTS

This work was financially supported by Grant No. 33620230101137CB from the Secretaría de Ciencia y Técnica of the Universidad Nacional de Córdoba (UNC), Argentina, and also through Grant No. PIP11220200100986CO from CONICET, Argentina. The authors are also grateful to the Laboratorio de Microscopía y Análisis por Rayos X (LAMARX-UNC), where the experimental determinations were performed.

DATA AVAILABILITY

The data that support the findings of this article are not publicly available. The data are available from the authors upon reasonable request.

---

[1] J. H. Scofield, *K*- and *L*-shell ionization of atoms by relativistic electrons, Phys. Rev. A **18**, 963 (1978).

[2] D. Bote and F. Salvat, Calculations of inner-shell ionization by electron impact with the distorted-wave and plane-wave Born approximations, Phys. Rev. A **77**, 042701 (2008).

[3] S. P. Limandri, A. Carreras, J. Trincavelli, J. Guzmán, D. Mitnik, C. Montanari, and S. Segui, Experimental cross sections for K-shell ionization by electron impact, At. Data Nucl. Data Tables **166**, 101756 (2025).

[4] X. Llovet, C. J. Powell, F. Salvat, and A. Jablonski, Cross sections for inner-shell ionization by electron impact, J. Phys. Chem. Ref. Data **43**, 013102 (2014).

[5] A. Aguilar, G. Castellano, S. Segui, J. Trincavelli, and A. Carreras, M-subshell X-ray production cross sections of Re and Os by electron impact, J. Anal. At. Spectrom. **38**, 751 (2023).

[6] M. Décima, G. Castellano, J. Trincavelli, and A. Carreras, X-ray production cross sections for Ir and Bi M-subshells induced by electron impact, Ultramicroscopy **259**, 113923 (2024).

[7] Y. K. Park, M. T. Smith, and W. Scholz, Cross sections for *L* x-ray production and *L*-subshell ionization by MeV electrons, Phys. Rev. A **12**, 1358 (1975).

[8] B. Schlenk, D. Berenyi, S. Ricz, A. Valek, and G. Hock, Electron impact L-shell ionization in the bombarding energy region from 300 to 600 keV, J. Phys. B **10**, 1303 (1977).

[9] S. Ricz, B. Schlenk, D. Berenyi, A. Valek, G. Hock, and S. S. el Nasr, L X-ray production cross section for Sm, Ho, Er and Bi at several hundred keV electron impact, J. Phys. B **11**, 4283 (1978).

[10] D. H. H. Hoffmann, C. Brendel, H. Genz, W. Löw, S. Müller, and A. Richter, Inner-shell ionization by relativistic electron impact, Z. Phys. A **293**, 187 (1979).

[11] L. M. Middleman, R. L. Ford, and R. Hofstadter, Measurement of cross sections for x-ray production by high-energy electrons, Phys. Rev. A **2**, 1429 (1970).

[12] K. Ishii, M. Kamiya, K. Sera, S. Morita, H. Tawara, M. Oyamada, and T. C. Chu, Inner-shell ionization by ultrarelativistic electrons, Phys. Rev. A **15**, 906 (1977).

[13] S. Reusch, H. Genz, W. Löw, and A. Richter, A method to determine L-subshell ionization cross sections for medium and heavy elements, Z. Phys. D **3**, 379 (1986).

[14] Z.-W. Wu, C.-J. Gou, D.-L. Yang, Z. An, X.-F. Peng, F.-Q. He, and Z.-M. Luo, L-shell X-ray production cross sections of Ta

and Tm by electron impact near the threshold region, Chin. Phys. Lett. **22**, 2538 (2005).

[15] G. Cheng-Jun, W. Zhang-Wen, Y. Dai-Lun, H. Fu-Qing, P. Xiu-Feng, A. Zhu, and L. Zheng-Ming, *L*-shell ionization cross section measurements of dysprosium and samarium by low-energy electron impact, Chin. Phys. Lett. **22**, 2244 (2005).

[16] Z. Wu, C. Gou, D. Yang, X. Peng, F. He, and Z. Luo, The L-shell ionization of Ho and Os induced by electron impact, Chin. Sci. Bull. **51**, 1929 (2006).

[17] Y. Wu, Z. An, Y. Duan, and M. Liu, Measurements of L-shell x-ray production cross-sections of Gd and W by low energy electron impact, J. Phys. B: At. Mol. Opt. Phys. **43**, 135206 (2010).

[18] J. Zhao, Z. An, J. J. Zhu, H. Huang, W. Tan, M. Liu, S. Bai, J. Lai, and X. Wang, L-subshell production cross sections of Lu and Hf by 10 keV-30 keV electron bombardment, Nucl. Instrum. Methods Phys. Res. Sect. B **562**, 165668 (2025).

[19] O. Gutfleisch, M. A. Willard, E. Brück, C. H. Chen, S. G. Sankar, and J. P. Liu, Magnetic Materials and Devices for the 21st century: Stronger, lighter, and more energy efficient, Adv. Mater. **23**, 821 (2011).

[20] A. Akah, Application of rare earths in fluid catalytic cracking: A review, J. Rare Earths **35**, 941 (2017).

[21] N. Zhang, H. Yan, L. Li, R. Wu, L. Song, G. Zhang, W. Liang, and H. He, Use of rare earth elements in single-atom site catalysis: A critical review—Commemorating the 100th anniversary of the birth of academician Guangxian Xu, J. Rare Earths **39**, 233 (2021).

[22] J. Henao and L. Martinez-Gomez, Review: on rare-earth perovskite-type negative electrodes in nickel–hydride (Ni/H) secondary batteries, Mater. Renew. Sustain. Energy **6**, 7 (2017).

[23] R. Bonetto, G. Castellano, and J. Trincavelli, Optimization of parameters in electron probe microanalysis, X-Ray Spectrom. **30**, 313 (2001).

[24] A. Carreras, G. Castellano, S. Segui, and J. Trincavelli, Experimental x-ray-production cross sections for the M_3, M_4, and M_5 subshells of Pt and Au by electron impact, Phys. Rev. A **102**, 012817 (2020).

[25] S. P. Limandri, M. A. Z. Vasconcellos, R. Hinrichs, and J. C. Trincavelli, Experimental determination of cross sections for *K*-shell ionization by electron impact for C, O, Al, Si, and Ti, Phys. Rev. A **86**, 042701 (2012).

[26] A. Sepúlveda, A. Bertol, M. Vasconcellos, J. Trincavelli, R. Hinrichs, and G. Castellano, Silver L_1, L_2 and L_3 cross-sections for ionization and x-ray production by electron impact, J. Phys. B: At. Mol. Opt. Phys. **47**, 215006 (2014).

[27] G. Castellano, J. Osán, and J. Trincavelli, Analytical model for the bremsstrahlung spectrum in the 0.25–20 keV photon energy range, Spectrochim. Acta Part B **59**, 313 (2004).

[28] V. Scott, G. Love, and S. Reed, *Quantitative Electron-Probe Microanalysis*, 2nd ed. (Horwood, London, 1995), pp. 40–41.

[29] R. H. Packwood and J. D. Brown, A Gaussian expression to describe $\phi(\rho z)$ curves for quantitative electron probe microanalysis, X-Ray Spectrom. **10**, 138 (1981).

[30] J. Riveros and G. Castellano, Review of $\varphi(\rho z)$ curves in electron probe microanalysis, X-Ray Spectrom. **22**, 3 (1993).

[31] S. J. B. Reed, Characteristic fluorescence corrections in electron-probe microanalysis, Br. J. Appl. Phys. **16**, 913 (1965).

[32] S. Limandri, A. Carreras, and J. Trincavelli, Effects of the carbon coating and the surface oxide layer in electron probe microanalysis, Microsc. Microanal. **16**, 583 (2010).

[33] W. Duane and F. L. Hunt, On x-ray wave-lengths, Phys. Rev. **6**, 166 (1915).

[34] J. A. Bearden, X-Ray Wavelengths, Rev. Mod. Phys. **39**, 78 (1967).

[35] S. T. Perkins, D. E. Cullen, M. H. Chen, J. H. Hubbell, J. Rathkopf, and J. H. Scofield, Tables and graphs of atomic subshell and relaxation data derived from the LLNL Evaluated Atomic Data Library (EADL), Z=1–100, Technical Report UCRL-50400, Vol. 30, Lawrence Livermore National Laboratory, Livermore, CA, 1991, https://doi.org/10.2172/10121422.

[36] J. Scofield, Hartree-Fock values of *L* x-ray emission rates, Phys. Rev. A **10**, 1507 (1974).

[37] G. F. Bastin, F. J. J. Van Loo, and H. J. M. Heijligers, Evaluation of the use of Gaussian $\phi(\rho z)$ curves in quantitative electron probe microanalysis: A new optimization, X-Ray Spectrom. **13**, 91 (1984).

[38] M. O. Krause, Atomic radiative and radiationless yields for *K* and *L* shells, J. Phys. Chem. Ref. Data **8**, 307 (1979).

[39] E. McGuire, Atomic L-shell Coster-Kronig, Auger, and radiative rates and flourescence yields for Na-Th, Phys. Rev. A **3**, 587 (1971).

[40] D. Bote, F. Salvat, A. Jablonski, and C. Powell, Cross sections for ionization of K, L and M shells of atoms by impact of electrons and positrons with energies up to 1 GeV: Analytical formulas, At. Data Nucl. Data Tables **95**, 871 (2009).

[41] S. Segui, M. Dingfelder, and F. Salvat, Distorted-wave calculation of cross sections for inner-shell ionization by electron and positron impact, Phys. Rev. A **67**, 062710 (2003).

[42] C. Mei, Y. Wu, Y. Yuan, C. Chang, Z. Qian, J. Zhu, and K. Moharram, Measurements of K-shell ionization cross sections of Al and L-shell x-ray production cross sections of Se by intermediate-energy electron impact, J. Phys. B: At. Mol. Opt. Phys. **49**, 245204 (2016).

[43] Y. Liang, M. Xu, Y. Yuan, Y. Wu, Z. Qian, C. Chang, C. Mei, J. Zhu, and K. Moharram, Lα and $M_{\alpha\beta}$ X-ray production cross-sections of Bi by 6–30 keV electron impact, Radiat. Phys. Chem. **141**, 17 (2017).

[44] S. F. Barros, V. R. Vanin, N. L. Maidana, M. N. Martins, J. A. García-Alvarez, O. C. B. Santos, C. L. Rodrigues, M. F. Koskinas, and J. M. Fernández-Varea, Ionization cross sections of the Au L subshells by electron impact from the L_3 threshold to 100 keV, J. Phys. B: At. Mol. Opt. Phys. **51**, 025201 (2018).

[45] S. F. Barros, V. R. Vanin, N. L. Maidana, A. A. Malafronte, J. M. Fernández-Varea, and M. S. Pindzola, Experimental and theoretical *L*-subshell ionization cross sections for ^{83}Bi by electron impact from the L_3 threshold to 100 keV, Phys. Rev. A **105**, 012818 (2022).

[46] J. Campbell, Fluorescence yields and Coster–Kronig probabilities for the atomic L subshells. Part II: The L1 subshell revisited, At. Data Nucl. Data Tables **95**, 115 (2009).